Materials Science-Poland, 37(2), 2019, pp. 289-295
http://www.materialsscience.pwr.wroc.pl/
DOI: 10.2478/msp-2019-0020

Adsorption and gas sensing properties of $CuFe_2O_4$ nanoparticles

MOHAMMAD ABU HAIJA[1], GEORGIA BASINA[2], FAWZI BANAT[2], AND AHMAD I. AYESH[3,*]

[1]Department of Chemistry, Khalifa University, SAN Campus, Abu Dhabi, United Arab Emirates
[2]Department of Chemical Engineering, Khalifa University, SAN Campus, Abu Dhabi, United Arab Emirates
[3]Department of Math., Stat. and Physics, Qatar University, Doha, Qatar

Spinel ferrite nanoparticles in the form $CuFe_2O_4$ were tested for gas sensing applications. Nanoparticles pressed in a disk form were used to construct conductometric gas sensors. The disk was placed between two electrical electrodes wherein the top electrode had a grid structure. The produced sensors were tested against H_2S and H_2 gases and they were found to be selective and sensitive to H_2S concentration as low as 25 ppm. The composition of the nanoparticles was confirmed by X-ray diffraction and energy dispersive X-ray spectroscopy measurements. The crystal structure was verified by both X-ray diffraction and transmission electron microscope. The observations obtained from the experiments demonstrated the high potential of using $CuFe_2O_4$ nanoparticles for H_2S sensing applications.

Keywords: *$CuFe_2O_4$; spinel ferrite; H_2S; gas sensor; nanoparticles*

1. Introduction

Spinel ferrites are defined as metal-ferrites with the general composition of MFe_2O_4, where M=Ni, Cu, Cd, Zn, etc. [1, 2]. They exhibit semiconducting properties since they are metal-oxide materials [3]. Nanoparticles of ferrite have been employed recently for different applications including gas sensing [4–7]. Since those nanoparticles are magnetic, they can be retrieved and recycled for further utilization. A special form of spinel ferrites is copper ferrite ($CuFe_2O_4$) which shows tetragonal symmetry and cubic close-packed crystal structure [8–10].

Nanoparticles of copper ferrites are particles of nanometer size that have chemical and physical characteristics which are dissimilar to their equivalent bulk material [11]. The main feature that determines gas sensing properties of ferrites is their large surface to volume ratio which indicates large number of surface reactive sites [11–13]. Upon exposure to a certain gas, ferrites react with the surface sites leading to a change in the surface electron density. Therefore, electrical conductance of nanoparticles is altered [14, 15]. The variation of electrical current signal reflects the concentration of the target gas. As such, this technique can be utilized to fabricate conductometric gas sensors that are accurate and easy to fabricate at low fabrication cost [16–18].

Pollution with H_2S gas is a major hazard and environment pollutant in petroleum production and fields related to transportation [19]. This gas is exceedingly poisonous to human and it is distinguished with its rotten egg odor [20]. Sensitive and selective H_2S sensors are essential for safety, control, and environment monitoring at crude oil production and refinery locations. Spinel ferrite nanoparticles have the potential to be utilized for industrial sensing of H_2S gas [21]. However, only few reports investigated the gas sensing properties of those nanoparticles [22, 23].

In this study, we investigated the possible use of $CuFe_2O_4$ nanoparticles for H_2S gas sensing applications. The morphology, structure, stability and composition were examined in detail using various techniques. The crystal structure was examined by both X-ray diffraction (XRD)

*E-mail: ayesh@qu.edu.qa

and transmission electron microscope (TEM). Gas sensors were produced using nanoparticle powder pressed in a disk form and placed between electrical electrodes with a grid structure. The produced sensors were tested against H_2S and H_2 gases. This work aimed to develop low cost and reliable H_2S gas sensors. Utilization of magnetic nanoparticles provides an important advantage as the nanoparticles can be collected and reused for further applications.

2. Experimental

2.1. Sensor fabrication

The sensor was fabricated by pressing the nanoparticle powder in a disk form using a hydraulic press at 20 MPa. The diameter of the disk was 13 mm. The disk was then provided with two electrodes: the bottom electrode was a sheet of Cu, and the top electrode was a stainless steel grid with the grid size 250 μm × 250 μm. The electrodes were connected electrically to wires by silver paste. The disk and electrodes assembly were fixed together by Scotch tape, where the exposed area of the disk to gas was 6 mm × 6 mm. The sensitivity measurements were performed inside a Teflon chamber with controlled temperature.

2.2. Sample characterization

Copper ferrite nanoparticle powder with purity of 98.5 % was purchased from Sigma-Aldrich. The composition and crystal structure of the nanoparticles were identified using XRD with a PANalytical powder diffractometer. The XRD measurements were performed using CuKα radiation at $\lambda = 1.5406$ Å operated at 40 kV and 40 mA. The XRD patterns were measured at a step size of 0.02° within a measurement range of $2\theta = 10°$ to 80°. A FEG (QUANTA-250) system that included a scanning electron microscope (SEM) and energy dispersive X-ray spectroscopy (EDS) were used to identify the morphology of nanoparticles and confirm their composition. In addition, a FEI (Tecnai-20) TEM was employed to determine nanoparticles size and to confirm their crystal structure using the electron diffraction planes. Herein, the nanoparticles were placed on carbon coated copper grid, and TEM measurements were performed using an accelerating voltage of 200 kV. Thermogravimetric analysis (TGA) conducted using a TA Instruments Q-series TGA system was used to investigate thermal stability of the nanoparticles.

H_2S adsorption testing was performed in a fixed bed U-shaped quartz reactor having a 4 mm internal diameter. 10 mg of the adsorbent was diluted with 200 mg of quartz particles after being sieved to sizes ranging between 125 μm and 250 μm. The mixture was placed inside the reactor between two layers of quartz wool. Pretreatment was conducted at 200 °C for 5 h, prior to each H_2S testing to remove all water and residuals under argon atmosphere, using argon gas (grade 5.0) with a flow rate of around 44 mL/min. Following, the reactor was cooled down to 150 °C, and the H_2S dissociative chemisorption took place under a pressure of 10^5 Pa using 99.1 ppm H_2S in N_2 stream and a flow rate of 42.5 mL/min. The effluents were then passed through 100 mg zeolite 3A (Sigma-Aldrich) bed to absorb water before being examined in a PerkinElmer Clarus 580 gas chromatograph (GC), model Arnel 4025PPC and model Arnel 4016PPC sulfur chemiluminescence detector (SCD). After the breakthrough took place, the GC argon gas was passed through the system to flush out any remaining H_2S.

The absorbent regeneration was achieved by calcination under oxygen stream (5 % O_2 in N_2, 41 m/min) at 500 °C for 7 h. Then it was cooled down to 150 °C following by argon flow in order to remove any physisorbed O_2, before the H_2S sorption experiment.

The sulfur capacity is defined as the total H_2S moles adsorbed per mass of adsorbent according to the following equations. The breakthrough point was determined when the H_2S concentration at the outlet exceeded 5 ppmv H_2S and the experiment was stopped at 100 ppmv H_2S at the outlet:

$$Sulfur\ capacity\ \left(\frac{mmol}{g}\right) = \\ = \frac{Total\ moles\ adsorbed\ of\ H_2S}{Mass\ of\ adsorbent} \times 10^{-3} \quad (1)$$

$$Total\ moles\ adsorbed\ of\ H_2S\ (mol) = \\ = (Breakthrough\ time) \times\ (\dot{n}\ of\ H_2S) \quad (2)$$

$$\dot{n}\ of\ H_2S\ \left(\frac{mol}{s}\right) = \frac{xP\dot{V}}{RT} \quad (3)$$

where ṅ is H_2S molar rate (mol/s), x is H_2S mole fraction, $\dot{V}$ is H_2S volume flow rate (L/s), P is pressure (kPa), R is a constant ($L{\cdot}kPa{\cdot}K^{-1}{\cdot}mol^{-1}$), and T is temperature (298 K).

Current-voltage (I-V) and gas sensitivity measurements were performed using a Keithley Instruments source measurement unit SMU-236 inside a temperature controlled Teflon chamber. A K-type thermocouple was used to measure the temperature of the disk. For sensitivity measurements, the target gas was mixed with air using Bronkhorst mass flowmeter (MFC) controlled by computer. Alongside, the electrical current was measured across the sensor electrodes while a constant voltage was applied. The measurement circuit is shown schematically in Fig. 1.

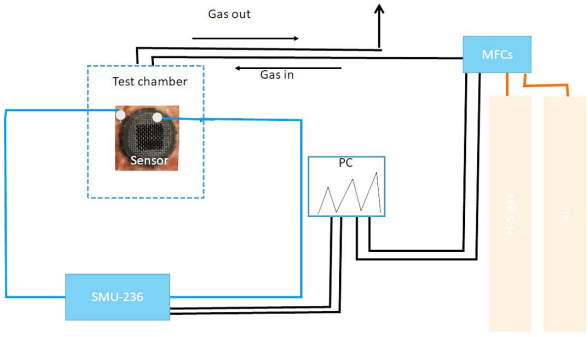

Fig. 1. Schematic diagram of the sensitivity measurement setup (not to scale) including the measurement circuit and the gas flow and control system.

3. Results and discussion

XRD was employed to analyze the crystallinity and structure of the $CuFe_2O_4$ nanopowder. Fig. 2 presents the XRD pattern of the nanopowder, which shows peaks at $2\theta = 18.4°$, 30.2°, 35.6°, 37.3°, 43.3°, 53.7°, 57.2°, 62.9°, and 74.4°. They are indexed to (1 1 1), (2 2 0), (3 1 1), (2 2 2), (4 0 0), (4 2 2), (5 1 1), (4 4 0), and (5 3 3) reflection planes of $CuFe_2O_4$, JCPDS 77-0010. The XRD pattern reveals a spinel cubic structure of the $CuFe_2O_4$ nanopowder [7, 24]. The average crystallite size was calculated using the Scherrer formula:

$$D = \frac{0.9\lambda}{\beta\ \cos\theta} \quad (4)$$

where λ is the wavelength in nm of the X-ray source, β is the peak width at half maximum in radian, θ is the diffraction angle, and D is the crystallite size in nm. Using Scherrer formula, the calculated crystallite size was determined as 29±1 nm.

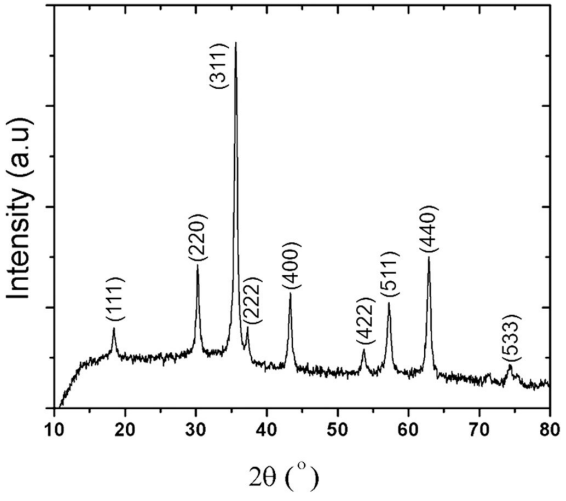

Fig. 2. XRD pattern of $CuFe_2O_4$ nanoparticles.

Fig. 3 shows a SEM image of the $CuFe_2O_4$ nanoparticles. The image shows spherical nanoparticles with an average size of 28±13 nm, which is consistent with the result obtained from XRD measurements. The inset of Fig. 3 shows the EDS results that confirm the composition of the nanoparticles. The morphology and composition have further been investigated using TEM as shown in Fig. 4. Fig. 4 confirms the nanoparticle size, and it reveals clear electron diffraction pattern. The measured lattice spaces are shown in Fig. 4b to Fig. 4g, and presented in Table 1 along with the associated Miller indices. Those indices are associated with spinel cubic structure of $CuFe_2O_4$ which is consistent with the XRD results.

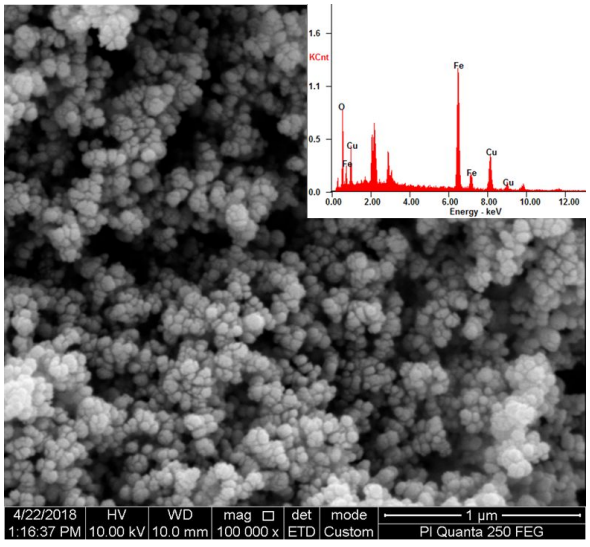

Fig. 3. SEM image of the $CuFe_2O_4$ nanoparticles. The inset shows the results of EDS analysis.

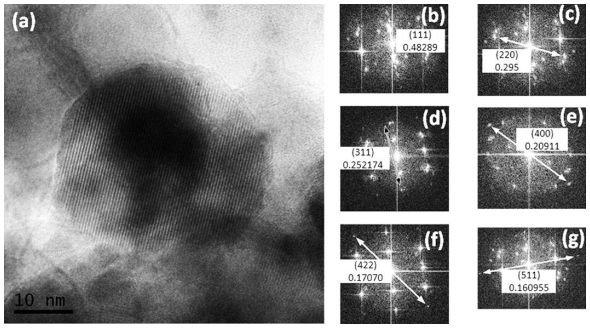

Fig. 4. (a) TEM images of $CuFe_2O_4$ nanoparticles showing electron diffraction planes; (b) to (g): lattice distances with the associated Miller indices.

Table 1. Lattice distances (d) and the associated Miller indices measured from the TEM images.

#	Miller indices from TEM	d [nm]
1	1 1 1	0.04289
2	2 2 0	0.29500
3	3 1 1	0.25210
4	4 0 0	0.20900
5	4 2 2	0.17070
6	5 1 1	0.16096

Thermal stability of the $CuFe_2O_4$ nanopowder at elevated temperatures was investigated by TGA, as presented in Fig. 5. The TGA curve of the nanopowder shows the mass loss in the temperature range between 25 °C and 550 °C. The curve suggests a thermally stable $CuFe_2O_4$ sample with a total weight loss of about 1 % only, part of which can be due to the evaporation of surface water molecules at elevated temperature.

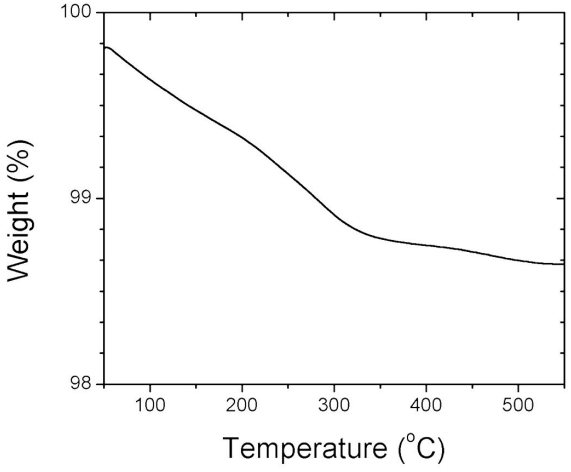

Fig. 5. TGA curve of $CuFe_2O_4$ nanoparticles between 25 °C and 550 °C.

Copper ferrites react with hydrogen sulfide at high temperatures (538 °C to 600 °C) promoting formation of chalcopyrite [25] through a stepwise reduction of $CuFe_2O_4$ and production of an intermediate compound of $CuFeO_2$ and then $CuFeS_2$, according to the following reaction [25]:

$$CuFeO_2 + H_2S \rightarrow CuFeS_2 + H_2O \qquad (5)$$

In this work, $CuFe_2O_4$ nanoparticles were tested as adsorbent for H_2S capture at low temperature. It is known, that breakthrough curves represent the time profile for saturation of a given amount of adsorbent [26]. Fig. 6 presents the H_2S breakthrough curves of $CuFe_2O_4$ particles after sulfidation (fresh cycle) at 150 °C (a) and following second cycle at 150 °C after regeneration (b). The breakthrough curves were recorded from the start of the flow until all the inflowing 100 ppm H_2S stream was detected at the GC. The horizontal axis shows the time in minutes needed for the breakthrough (5 ppm) and the y-axis shows the H_2S concentration at the outlet. From the obtained breakthrough curves, the breakthrough time

has been determined to be 430 min and 390 min respectively at 5 ppmv for the fresh and the second sulfidation cycle at 150 °C after regeneration with a computed sulfur capacity of 8.9 mmol/g (a) and 7.5 mmol/g (b). The sulfur capacity of 7.5 mmol/g reveals, according to the literature [25], a conversion of $CuFe_2O_4$ to $CuFeS_2$ by approximately 84 % compared to the initial capacity of the fresh sulfidation of 8.9 mmol/g at 150 °C, indicating a reduction of 16 %.

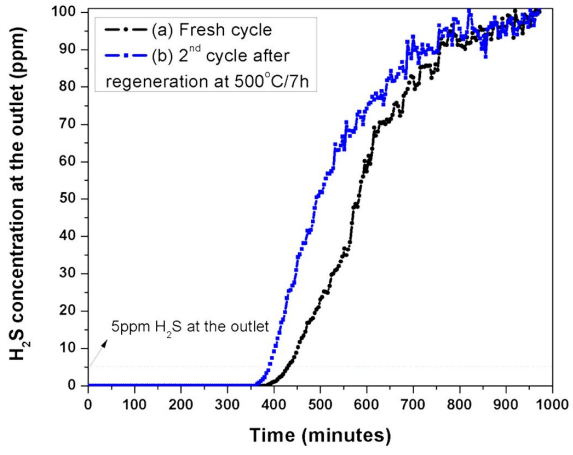

Fig. 6. Breakthrough curves of H_2S over $CuFe_2O_4$ (a) fresh sulfidation cycle at 150 °C and (b) second sulfidation cycle at 150 °C, after regeneration at 500 °C for 7 h.

The gas response is defined as:

$$S = \frac{|I_{gas} - I_0|}{I_0} \times 100\%, \qquad (6)$$

where I_0 and I_{gas} are the electrical currents of the sensor upon exposure to air and the target gas, respectively. The gas response measurements for H_2S are presented in Fig. 7a. The plots reveal that the gas sensor is functional at 140 °C, and it can detect a minimum H_2S concentration of 25 ppm at 200 °C. The sensor was tested against H_2 gas, and the results are presented in Fig. 7b. Fig. 7b shows that the sensor response to hydrogen is lower than that of H_2S. Also the sensor is functional at high concentrations, ∼50000 ppm, of H_2 only at high temperatures. Therefore, the present sensor is more selective to H_2S as compared with H_2.

Sensor response time is known as the time needed for the response to reach 90 % of its maximum value. The response time measurements are presented in Fig. 8 for both H_2S and H_2 gases. The error bars are taken as the standard deviation for the response time at different gas concentrations. Fig. 8 reveals that the response time does not change with temperature within the error bars. The average values of the response times over different temperatures are 34±23 s and 35±14 s for H_2S and H_2 gases, respectively. Those times are considered as relatively fast response times as compared with the previously reported values for similar sensors [5, 7, 27].

Gas sensing by nanoparticles is associated with the number of reactive sites on the nanoparticle surface. This process is mainly assigned to the adsorption of oxygen species (such as O^- and O^{2-}) [7] on the nanoparticle surface. Herein, the adsorption process perturbs the surface charge, thus, electrical conductivity and resistance. Oxygen adsorption process is described by the following equations (where the "ads" denotes the adsorbed ions of oxygen) [7, 18, 28]:

$$H_2S + 3O^-(ads) \rightarrow H_2O + SO_2 + 3e^- \qquad (7)$$

$$H_2S + 3O^{2-}(ads) \rightarrow H_2O + SO_2 + 6e^- \qquad (8)$$

Here, the oxygen ions adsorbed on the nanoparticle reactive sites are the main contributors in the gas sensor mechanism. Upon adsorption, metal reduction causes release of electrons to the conduction band of nanoparticles, thus, electrical conductivity increases by a value that is proportional to the number of released electrons [5]. The operation temperature of a sensor is mainly affected by two main processes: speed of reaction with the target gas at low temperature, and speed of gas molecules diffusion at high temperatures [7, 29]. Therefore, the value of operation temperature of a sensor controls the quantity of adsorbed gas molecules on the surface of nanoparticles. A low sensor response at low operation temperatures is caused by the fact that gas molecules have too low thermal energy

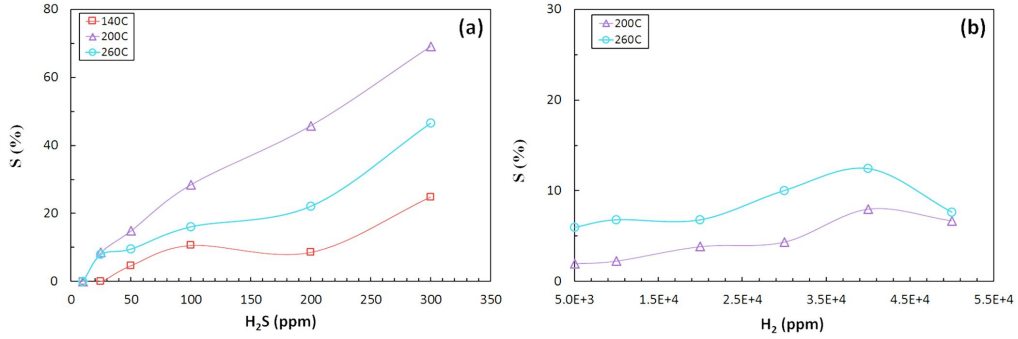

Fig. 7. Gas response measurements of $CuFe_2O_4$ based sensor for: (a) H_2S, and (b) H_2.

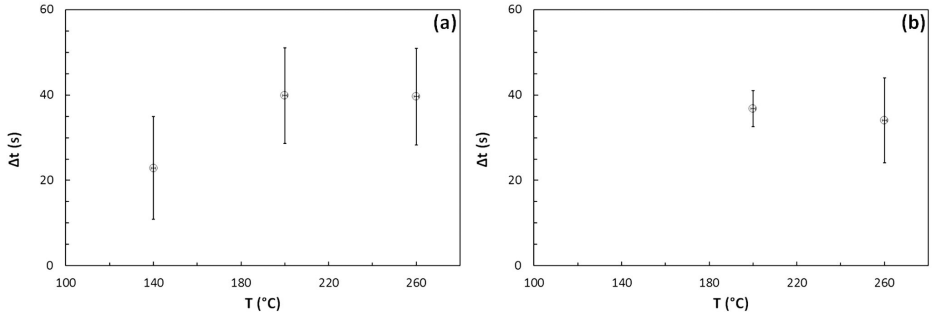

Fig. 8. Sensor response time measurements for: (a) H_2S, and (b) H_2.

to enable reaction with the adsorbed ions of oxygen on the nanoparticle surface. At high temperatures, the thermal energy increases which allows gas molecules to overcome the barrier of activation energy and establish reaction on nanoparticle surface. In addition, both electron concentration as well as electrical conductivity increase at high temperatures because of the high conversion of adsorbed oxygen ions [29, 30]. Thus, the sensor response increases at high operating temperatures. It is worthy to note that the optimum gas response of a sensor is obtained when speeds of both reaction and diffusion are maximum. Therefore, the optimum operating temperature is dependent on the nanoparticle composition and gas type.

4. Conclusions

In conclusion, conductometric gas sensors based on $CuFe_2O_4$ nanoparticles are reported in this work. The sensors are made in a form of a disk provided with two electrodes. The produced sensors are selective to H_2S gas and sensitive to its low concentration of 25 ppm at 140 °C. The crystal structure of the nanoparticles is spinel cubic as confirmed by XRD and TEM analysis. The produced sensors are environmentally friendly, low cost, and reliable. In addition, the nanoparticles are reusable since they are magnetic. Therefore, $CuFe_2O_4$ nanoparticles are potentially interesting in environmental and industrial sensing applications.

Acknowledgements

This work was supported by the Khalifa University under the Grant Number RIFP-14312 and the Qatar University under the Grant Number QUCG-CAS-2018\2019-1.

References

[1] ZEESHAN T., ANJUM S., IQBAL H., ZIA R., *Mater. Sci.-Poland*, 36 (2018), 255.

[2] NETHALA G.P., TADI R., ANUPAMA A.V., SHINDE S.L., VEERAIAH V., *Mater. Sci.-Poland*, 36 (2018), 310.

[3] JAHAN N., ZAKARIA A., *Mater. Sci.-Poland*, 34 (2016), 185.

[4] CHEN N.-S., YANG X.-J., LIU E.-S., HUANG J.-L., *Sensor. Actuat. B-Chem.*, 66 (2000), 178.
[5] HAIJA M.A., AYESH A.I., AHMED S., KATSIOTIS M.S., *Appl. Surf. Sci.*, 369 (2016), 443.
[6] RANJITH KUMAR E., JAYAPRAKASH R., SARALA DEVI G., SIVA PRASADA REDDY P., *Sensor. Actuat. B-Chem.*, 191 (2014), 186.
[7] HAIJA M.A., ABU-HANI A.F.S., HAMDAN N., STEPHEN S., AYESH A.I., *J. Alloy. Compd.*, 690 (2017), 461.
[8] TAO S., GAO F., LIU X., TOFT SØRENSEN O., *Mater. Sci. Eng. B-Adv.*, 77 (2000), 172.
[9] AMER M.A., MEAZ T., HASHHASH A., ATTALAH S., FAKHRY F., *J. Alloy. Compd.*, 649 (2015), 712.
[10] RANJITH KUMAR E., JAYAPRAKASH R., KUMAR S., *J Magn Magn Mater*, 351 (2014), 70.
[11] KRUIS F.E., FISSAN H., PELED A., *J. Aerosol. Sci.*, 29 (1998), 511.
[12] AYESH A.I., MAHMOUD S.T., AHMAD S.J., HAIK Y., *Mater. Lett.*, 128 (2014), 354.
[13] AYESH A.I., QAMHIEH N., MAHMOUD S.T., ALAWADHI H., *J. Mater. Res.*, 27 (2012), 2441.
[14] KOROTCENKOV G., *Mater. Sci. Eng. R-Rep.*, 61 (2008), 1.
[15] YAN H., SONG P., ZHANG S., YANG Z., WANG Q., *J. Alloy. Compd.*, 662 (2016), 118.
[16] BARSAN N., KOZIEJ D., WEIMAR U., *Sensor. Actuat. B-Chem.*, 121 (2007), 18.
[17] AYESH A.I., KARAM Z., AWWAD F., MEETANI M.A., *Sensor. Actuat. B-Chem.*, 221 (2015), 201.
[18] AYESH A.I., ABU-HANI A.F.S., MAHMOUD S.T., HAIK Y., *Sensor. Actua.t B-Chem.*, 231 (2016), 593.
[19] HANKARE P.P., JADHAV S.D., SANKPAL U.B., PATIL R.P., SASIKALA R., MULLA I.S., *J. Alloy. Compd.*, 488 (2009), 270.
[20] KIMURA H., *Neurochem. Int.*, 63 (2013), 492.
[21] SUMANGALA T.P., MAHENDER C., BARNABE A., VENKATARAMANI N., PRASAD S., *J. Magn. Magn. Mater.*, 418 (2016), 48.
[22] BAVANDPOUR R., KARIMI-MALEH H., ASIF M., GUPTA V.K., ATAR N., ABBASGHORBANI M., *J. Mol. Liq.*, 213 (2016), 369.
[23] RANJITH KUMAR E., SIVA PRASADA REDDY P., SARALA DEVI G., SATHIYARA J., *J. Magn. Magn. Mater.*, 398 (2016), 281.
[24] HAMDAN N., ABU HAIJA M., BANAT F., ESKHAN A., *Desalin. Water Treat.*, 69 (2017), 268.
[25] FLYTZANI-STEFANOPOULOS S.S.T.M., GAVALAS G.R., BAGAJEWICZ, SHARMA P.K., *Energ. Fuel*, 190 (1985), 1155.
[26] SHANG G., LIU L., CHEN P., SHEN G., LI Q., *J. Air Waste Mange.*, 66 (2016), 439.
[27] AYESH A.I., ABU-HANI A.F.S., MAHMOUD S.T., HAIK Y., *Sensor. Actuat. B-Chem.*, 231 (2016), 593.
[28] MENG F.-N., DI X.-P., DONG H.-W., ZHANG Y., ZHU C.-L., LI C., CHEN Y.-J., *Sensor. Actuat. B-Chem.*, 182 (2013), 197.
[29] GADKARI A.B., SHINDE T.J., VAVAMBEKAR P.N., FERRITE GAS SENSORS, *IEEE Sens. J.*, 11 (2011), 849.
[30] AYESH A.I., HAIJA M.A., SHAHEEN A., BANAT F., *Appl. Phys. A-Mater.*, 123 (2017), 682.

Received 2018-11-21
Accepted 2019-03-11